On the Derivation of Volume Decorrelation From TanDEM-X Bistatic Coherence

Paola Rizzoli, Luca Dell'Amore, José-Luis Bueso-Bello, Nicola Gollin, Daniel Carcereri, and Michele Martone

***Abstract*—The bistatic interferometric coherence is affected by different sources of error, among which volume decorrelation, which quantifies the amount of noise caused by volume scattering mechanisms. This represents a key quantity not only for the performance assessment of interferometric synthetic aperture radar (SAR) products, but also for a large variety of scientific applications, ranging from land cover classification to physical parameters estimation, such as ice structure, forest height, and biomass retrieval. The magnitude of volume decorrelation can be derived from the total interferometric coherence by properly compensating for all other decorrelation sources. Considering that temporal decorrelation can be neglected for a bistatic system such as TanDEM-X, the remaining decorrelation components can be estimated from the SAR scene characteristics and the system parameters. In the scientific community, it is a common practice to approximate the volume decorrelation with the coherence or to compute it by compensating for the signal-to-noise ratio (SNR) decorrelation only, which typically represents the predominant decorrelation component. The aim of this work is to assess the impact of different decorrelation sources in detail and to provide the readers with a practical procedure for a precise computation of the volume decorrelation from TanDEM-X bistatic data. In particular, we concentrate on the two most relevant decorrelation components: the SNR and the quantization components. Regarding the former, we estimate the noise equivalent sigma naught directly from real SAR data and we provide the users with a set of polynomial coefficients for the retrieval of the system noise floor for each operational TanDEM-X StripMap beam used for the generation of the global digital elevation model. These values are then combined with the backscatter for the retrieval of the scene-based SNR and of the corresponding decorrelation. Concerning the latter, we analyze its dependence on the backscatter local statistics and quantization rate and we provide the reader with a set of empirical lookup tables for quantifying its impact on the coherence. Finally, we provide reasonable assumptions for all other remaining decorrelation sources, discussing two application scenarios in the fields of forest mapping and forest height estimation, which demonstrate the added value of the proposed methodology.**

***Index Terms*—Bistatic coherence, SAR interferometry, synthetic aperture radar (SAR), TanDEM-X, volume decorrelation.**

Manuscript received October 27, 2021; revised March 18, 2022; accepted April 19, 2022. Date of publication April 26, 2022; date of current version May 11, 2022. *(Corresponding author: Paola Rizzoli.)*

The authors are with the Microwaves and Radar Institute, German Aerospace Center, 82234 Wessling, Germany (e-mail: Paola.Rizzoli@dlr.de; luca.dellamore@dlr.de; Jose-Luis.Bueso-Bello@dlr.de; Nicola.Gollin@dlr.de; daniel.carcereri@dlr.de; Michele.Martone@dlr.de).

Digital Object Identifier 10.1109/JSTARS.2022.3170076

I. Introduction

THE total interferometric coherence γ_{Tot} represents the key quantity for assessing the quality of a synthetic aperture radar (SAR) interferogram [1], [2]. It is defined as the normalized cross-correlation coefficient between the interferometric image pair as

$$\gamma_{\text{Tot}} = \frac{|E[u_1 \cdot u_2^*]|}{\sqrt{E[|u_1|^2] \cdot E[|u_2|^2]}} \tag{1}$$

where $E[\cdot]$ represents the statistical expectation, $*$ the complex conjugate operator, and $|\cdot|$ the absolute value. u_1 and u_2 identify the master and slave images, respectively. γ_{Tot} varies between 0 and 1 and it is typically estimated from real SAR data by applying a sliding boxcar window W centered around the considered pixel of indices $[i, j]$ as

$$\hat{\gamma}_{\text{Tot}}[i,j] = \frac{\left|\sum_W u_1[i,j] \cdot u_2^*[i,j]\right|}{\sqrt{\sum_W |u_1[i,j]|^2 \cdot \sum_W |u_2^*[i,j]|^2}}. \tag{2}$$

Please note that the hat symbol $\hat{}$ will be utilized throughout this article to identify decorrelation components that contribute to the total estimated coherence $\hat{\gamma}_{\text{Tot}}$ and that the indices $[i, j]$ will be omitted for the sake of brevity.

We now consider the coherence factorization presented in [3] and extended in [4], having

$$\gamma_{\text{Tot}} = \gamma_{\text{Amb}} \cdot \gamma_{\text{Rg}} \cdot \gamma_{\text{Az}} \cdot \gamma_{\text{Temp}} \cdot \gamma_{\text{Quant}} \cdot \gamma_{\text{SNR}} \cdot \gamma_{\text{Vol}} \tag{3}$$

where the terms on the right-hand side are, hereby, called *decorrelation factors*. They account for different error contributions related to SAR ambiguities (γ_{Amb}), coregistration errors in range and baseline decorrelation (γ_{Rg}), misregistration in azimuth and relative shift of the Doppler spectra (γ_{Az}), temporal decorrelation (γ_{Temp}), quantization (γ_{Quant}), thermal noise (γ_{SNR}), and volume decorrelation (γ_{Vol}). The first three terms (γ_{Amb}, γ_{Rg}, and γ_{Az}) are mainly related to the specific sensor parameters and acquisition geometry [5], while γ_{Temp}, γ_{Quant}, γ_{SNR} and γ_{Vol} show a dependence on the specific characteristics of the illuminated scene on the ground, and consequently, on the kind of underlying backscattering mechanism.

In particular, γ_{Temp} identifies the coherence loss caused by changes in the illuminated scene occurred between the two SAR acquisitions forming the interferometric pair [6]. In the specific case of bistatic InSAR data, such as TanDEM-X, $\gamma_{\text{Temp}} = 1$ since both master and slave images are simultaneously acquired [4].

γ_{Quant} quantifies the decorrelation caused by quantization of the raw data signal. Typically, quantization errors are nonlinear and signal-dependent distortions. They are often approximated as additive white Gaussian noise, but it has been demonstrated that their impact is strongly influenced by backscatter local statistics [7].

γ_{SNR} depends on the signal-to-noise ratio S of both master (S_{M}) and slave (S_{S}) acquisitions as [4]

$$\gamma_{\text{SNR}} = \frac{1}{\sqrt{(1+S_{\text{M}}^{-1})\cdot(1+S_{\text{S}}^{-1})}}. \tag{4}$$

The last decorrelation factor, γ_{Vol}, quantifies the coherence loss in the presence of volumetric scattering. This phenomenon occurs, e.g., when radar waves penetrate into forest canopies or ice and snow-covered regions. The amount of penetration, and therefore, of decorrelation depends on several factors such as the radar frequency, the acquisition geometry, and the target characteristics. Regarding the bistatic acquisition geometric parameters, γ_{Vol} is closely related to the height of ambiguity h_{amb}, which depends on the orthogonal baseline $B_{\perp}$ between the master and slave sensors. For the bistatic case, it is defined as

$$h_{\text{amb}} = \frac{\lambda \cdot r \cdot \sin\theta}{B_{\perp}} \tag{5}$$

being λ the wavelength, r the slant range, and θ the incidence angle [8]. The volume decorrelation factor can finally be directly derived from the interferometric coherence by inverting (3) as

$$\gamma_{\text{Vol}} = \frac{\gamma_{\text{Tot}}}{\gamma_{\text{Amb}}\cdot\gamma_{\text{Rg}}\cdot\gamma_{\text{Az}}\cdot\gamma_{\text{Temp}}\cdot\gamma_{\text{Quant}}\cdot\gamma_{\text{SNR}}}. \tag{6}$$

γ_{Vol} is clearly linked to the intrinsic structure of the illuminated volumetric target and represents a valuable input for a large variety of practical applications. For example, its approximation through the interferometric coherence has been used for model-based inversion of forest parameters, such as tree height [9]–[12] and forest structure [13], [14], or for the estimation of the radar penetration bias into volumetric targets [15].

Between 1995 and 2000, the ERS-1/2 mission [16] of the European Space Agency provided repeat-pass InSAR data at only one-day revisit-time, by utilizing two C-band satellites (ERS-1 and ERS-2) flying on the same orbital plane. Since it allowed for a significant reduction of temporal decorrelation phenomena, this was for years the reference spaceborne mission for the development of InSAR coherence-based applications, related, e.g., to forest biomass retrieval [17] or to the estimation of radar penetration into snow-covered regions [18] and snow depth [19]. The first spaceborne bistatic images were acquired in 2000 at C and X band by the Shuttle Radar Topography Mission [20] and allowed for the computation of the bistatic coherence at a fixed physical baseline of 60 m, corresponding to the length of the mast between the main antenna (transmit and receive), mounted on the NASA Space Shuttle, and the outboard antenna (receive only) mounted at the extremity of the mast itself.

Currently, the TanDEM-X mission is the only spaceborne bistatic SAR mission, which operationally provides single-pass InSAR acquisitions at X band with variable baselines, polarizations, and acquisition modes [4], [21]. It comprises two twin satellites, namely TerraSAR-X (TSX) and TanDEM-X (TDX) launched in 2007 and 2010, respectively, which fly in a close orbit configuration. Throughout the entire mission duration, the bistatic coherence has represented the key parameter for monitoring the global interferometric performance and it has been exhaustively investigated [22]–[24]. Since the TanDEM-X coherence is unaffected by temporal decorrelation, it is, therefore, possible to isolate the volume decorrelation factor from all other sources of coherence loss. In this scenario, many scientific works have been developed and published thanks to the available TanDEM-X bistatic datasets. For example, in the field of biosphere-related applications, it is widely used for tree height [25]–[32] and above-ground biomass estimation [33]–[37]. It represents a useful input feature for the retrieval of vegetation height in agricultural areas [38], [39] as well as for crop type mapping [40]. Moreover, the added value of the bistatic coherence has been demonstrated for extended land cover classification and forest mapping purposes as well [41]–[44]. Similarly, in the field of cryosphere-related applications, TanDEM-X bistatic datasets have been used for the estimation of the radar penetration depth and for the classification of diagenetic snow facies [45]–[48].

To our knowledge, most of the scientific works published in the literature, which make use of the TanDEM-X volume decorrelation factor, simply rely on the interferometric coherence or compute $\hat{\gamma}_{\text{Vol}}$ by compensating for the $\hat{\gamma}_{\text{SNR}}$ component only, i.e., $\hat{\gamma}_{\text{Vol}} \simeq \hat{\gamma}_{\text{Tot}}/\hat{\gamma}_{\text{SNR}}$ (e.g., [25], [27], [31], and [32]). This is quite a rough approximation, since other factors, and in particular, $\hat{\gamma}_{\text{Quant}}$, play a nonnegligible role, risking to significantly bias the estimation of $\hat{\gamma}_{\text{Vol}}$ [7]. Moreover, the estimation of the system noise floor for computing the signal-to-noise ratio in TanDEM-X products needs some additional remarks as well, which are detailed further on in this article. Out of all the previously mentioned works, we found that only the ones presented in [8], [40], and [42]–[45] rely on an estimate of the volume decorrelation factor $\hat{\gamma}_{\text{Vol}}$, derived by compensating for all other decorrelation terms under some practical assumptions, such as the utilization of the theoretical system noise floor and a rough estimation of $\hat{\gamma}_{\text{Quant}}$.

In the following sections, we concentrate on the two most relevant aspects for retrieving the estimate of the volume decorrelation factor $\hat{\gamma}_{\text{Vol}}$ from the estimated coherence $\hat{\gamma}_{\text{Tot}}$, i.e., the computation of $\hat{\gamma}_{\text{SNR}}$ and $\hat{\gamma}_{\text{Quant}}$, and we provide practical procedures for the use of operational TanDEM-X single-polarization (HH) StripMap data. Particularly, in Section II, we concentrate on the estimation of the noise equivalent sigma naught for all considered beams through distributed target analyses on real data. This parameter is required for the computation of the image SNR, and subsequently, of $\hat{\gamma}_{\text{SNR}}$. In Section III, we analyze the impact of block-adaptive quantization (BAQ) [49], which is the quantization scheme applied to TanDEM-X raw data, on the coherence degradation depending on local backscatter statistics and we derive and validate a series of lookup tables (LUTs) for the estimation of $\hat{\gamma}_{\text{Quant}}$. Section IV briefly reports on all other decorrelation sources, while Section V presents the output

product, discussing two possible application scenarios in the fields of forest mapping and forest height estimation, which aim at confirming the utility of the proposed method. Finally, Section VI concludes this article.

II. SNR Decorrelation Factor

The SNR decorrelation factor $\hat{\gamma}_{\text{SNR}}$ is computed as in (4). The ratio S is evaluated for the master (S_{M}) and slave (S_{S}) images, separately, as

$$S = \frac{\beta^0(\theta) - \beta^n(\theta)}{\beta^n(\theta)} \tag{7}$$

being $\beta^0(\theta)$ and $\beta^n(\theta)$ the radar brightness and the noise equivalent beta naught of either the master or the slave image, respectively. We choose to express this ratio in terms of radar brightness instead of backscattering coefficient in order to avoid the practical calculation of the local incidence angle, as shown in the following, which might introduce further uncertainties in case of a limited knowledge of the underlying topography [50].

To evaluate (7), we consider the radar brightness $\beta^0(\theta)$ of either the master or the slave image, which is retrieved through the absolute calibration of the focused data as

$$\beta^0(\theta) = \frac{(DN(\theta))^2}{K} \tag{8}$$

being DN the recorded digital number and K the absolute calibration constant.[1]

One should notice that the radar brightness $\beta^0(\theta)$ and the backscattering coefficient $\sigma^0(\theta)$ are directly related as [52]

$$\beta^0(\theta) = \frac{\sigma^0(\theta)}{\sin\theta_l} \tag{9}$$

where θ_l is the local incidence angle, while θ is the slant range-dependent incidence angle of the image pixel, which shows a monotonic increase from near to far range. The local incidence angle is computed as $\theta_l = \theta - \alpha$, where α represents the terrain local slope and it can be derived from an underlying DEM and the satellite orbit position.

The system noise floor is typically evaluated in terms of noise equivalent sigma naught $\sigma^n(\theta)$ by the scientific community. It identifies the scattering coefficient for which the clutter-to-noise ratio (CNR) is equal to one. Given its wide use, we decided to keep this formulation for the estimation of the noise floor profiles from real TanDEM-X data, in order to make them directly comparable to noise profiles from the product annotation as well as from the theoretical mission performance, but we then rely on the noise equivalent beta naught for the computation of the SNR as in (7). To this aim, we follow the same principle of (9) so that $\beta^n(\theta)$ can be derived from $\sigma^n(\theta)$ as

$$\beta^n(\theta) = \frac{\sigma^n(\theta)}{\sin\theta_l} \tag{10}$$

[1]In order to avoid confusion, please consider that this is the theoretical formulation of the SAR absolute calibration, while the specific TSX/TDX calibration factor included in the product annotation has to be applied through a multiplication operator [51].

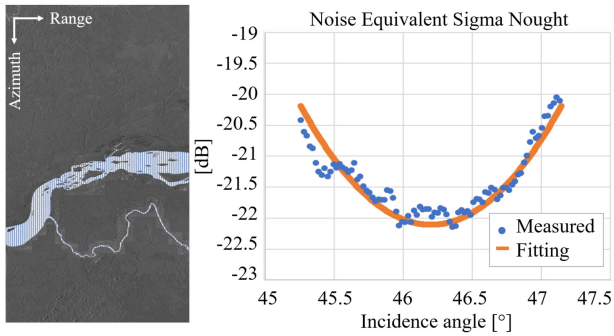

Fig. 1. Example of noise equivalent sigma naught estimation for the tandem_a1_080 beam using TerraSAR-X satellite data. (a) Exemplary backscatter image and detected water surfaces, subdivided into neighbor segments in the slant-range dimension (blue). (b) Measured minimum backscatter for all the considered segments from the five acquisitions with lowest backscatter levels (blue) and second-order polynomial fitting (orange).

where, in practice, it is reasonable to assume $\theta \simeq \theta_l$ since the estimation of the noise equivalent sigma naught from real SAR data is typically performed over flat areas leading to $\alpha = 0$, as explained in the following.

The noise equivalent sigma naught depends on the instrument parameters and shows a slant-range, beam-dependent profile that is inversely proportional to the shape of the antenna pattern. As mentioned previously, it can be either theoretically computed as in [4], retrieved from dedicated noise pulses or directly estimated from focused data, by extracting the mean backscattering coefficient of distributed targets characterized by low reflectivity. This is the case, e.g., of calm water surfaces, where a specular reflection of the radar wave occurs and a negligible backscattered signal is recorded by the sensor. We utilize this last approach to estimate the noise floor of all considered TanDEM-X beams used for the generation of the global DEM, acquired in single-polarization (HH) with 100-MHz range bandwidth. To do so, we consider different test areas located in Brazil, where all overlapping TanDEM-X beams are crossed in the slant-range direction by the Amazon river. Fig. 1 shows an example of $\sigma^n(\theta)$ estimation for the tandem_a1_080 beam, corresponding to an incidence angle interval between 45.2° and 47.2°. Here, the measured $\hat{\sigma}^n(\theta)$ profile is evaluated by first dividing the $\sigma^0(\theta)$ backscatter image into adjacent sectors along the slant-range dimension, and then, by selecting only those pixels classified as water. In order to properly detect water surfaces, we applied a watershed-based segmentation algorithm, as already done for the generation of the global TanDEM-X water body layer [53], [54]. The result is shown in Fig. 1(a). Then, we repeated the procedure over at least 15 acquisitions (not necessarily acquired over the same area on ground), and for each sector, we considered the minimum recorded value of backscatter, in order to obtain a reliable estimate of the system noise floor. Afterwards, a second-order polynomial is fitted to such values of $\sigma^0(\theta)$ (in decibel unit), and the estimated noise equivalent sigma naught $\hat{\sigma}^n(\theta)$ is retrieved as

$$\hat{\sigma}^n(\theta) = c_2 \cdot \theta^2 + c_1 \cdot \theta + c_0 \tag{11}$$

TABLE I
SECOND-ORDER POLYNOMIAL FITTING COEFFICIENTS FOR THE COMPUTATION OF $\hat{\sigma}^n(\theta)$ PROFILES AS IN (11) FOR ALL CONSIDERED TANDEM-X SINGLE-POLARIZATION (HH) STRIPMAP BEAMS OF THE TERRASAR-X (TOP) AND TANDEM-X (BOTTOM) SATELLITES (WHERE, FOR THE SAKE OF BREVITY, THE PREFIX TANDEM_ IS OMITTED FROM THE BEAM IDENTIFIER)

TerraSAR-X

Beam	a1_000	a1_010	a1_020	a1_030	a1_040	a1_050	a1_060	a1_070	a1_080	a1_090
c_2	2.5029	2.4096	2.5404	2.8325	1.692	2.9125	2.2981	1.1263	1.5713	2.0185
c_1	-143.0223	-150.0801	-171.4327	-204.1159	-129.4081	-236.1618	-195.0404	-99.525	-144.9082	-191.973
c_0	2018.9713	2313.0669	2867.2076	3652.619	2451.0182	4763.4114	4114.1361	2174.0878	3316.7479	4540.4044
Beam	a2_005	a2_015	a2_025	a2_035	a2_045	a2_055	a2_065	a2_075	a2_085	a2_095
c_2	1.9048	2.8891	2.5407	2.0786	2.1742	2.8553	1.7467	2.4929	2.491	1.5663
c_1	-113.6816	-187.3507	-176.1178	-154.4814	-170.5357	-236.1952	-151.1212	-223.9492	-233.7805	-150.4794
c_0	1672.2722	3011.9486	3027.527	2846.911	3320.6003	4860.9355	3245.5738	5006.4705	5461.1267	3592.1568

TanDEM-X

Beam	a1_000	a1_010	a1_020	a1_030	a1_040	a1_050	a1_060	a1_070	a1_080	a1_090
c_2	2.3448	2.3491	2.0412	2.8201	1.6822	2.9532	1.2598	2.8248	1.3674	1.5649
c_1	-134.1576	-146.4362	-138.1778	-203.0806	-129.2035	-239.4561	-107.1426	-250.1493	-125.9624	-148.885
c_0	1894.3855	2258.5491	2313.3569	3631.8774	2457.2604	4829.7854	2255.3207	5512.9854	2876.938	3517.3485
Beam	a2_005	a2_015	a2_025	a2_035	a2_045	a2_055	a2_065	a2_075	a2_085	a2_095
c_2	2.0632	2.9575	2.6225	1.656	1.9947	3.1489	2.1367	2.4686	3.5245	1.4406
c_1	-123.1558	-191.8098	-181.7323	-123.0632	-156.6188	-260.4474	-184.9317	-221.8082	-328.9897	-138.1868
c_0	1813.7252	3084.8753	3123.6768	2263.5058	3051.1742	5361.6985	3978.3812	4958.6954	7653.7796	3291.2971

where θ is expressed in degrees of arc and $[c_0, c_1, c_2]$ are the fitting coefficients. The result is presented in Fig. 1(b). Please note that the fitting procedure is directly performed in decibel.

For the analysis, the incidence angle has been derived from the satellite look angle with respect to the WGS84 Ellipsoid and no local topography has been considered. This choice does not bias the results since flat terrain regions only are considered, as already commented for the computation of (10). Moreover, it is worth mentioning that a second-order polynomial is sufficient for a reliable fitting of the considered TanDEM-X beams, since no specific tapering of the antenna pattern in range is applied. The polynomial order might have to be increased otherwise, in order to properly follow the shape of the antenna pattern in the presence of multiple ripples, as in the case, e.g., of near-range beams of the TerraSAR-X mission (from Strip_001 to Strip_007).

In addition, one has to be aware that the noise equivalent sigma naught measured from the distributed target analysis can be biased by a noise contribution caused by the lossy quantization of the SAR raw data. The data-takes considered in this investigation were all compressed using BAQ at a rate of 3 bits/sample, which is the compression rate selected for nominal TanDEM-X acquisitions. In [7], it has been demonstrated that the use of such a quantization setting implies a noise floor increase of about 0.3 dB with respect to the BAQ-bypass case for all TanDEM-X beams (i.e., raw data are compressed using 8-bits analog-digital-converter (ADC), for which, in turn, the increase of noise can be reasonably neglected). According to these findings, we compensated for this effect by consistently subtracting 0.3 dB from the measured noise equivalent sigma naught profiles (i.e., from the c_0 coefficient).

Overall, we considered all 20 TanDEM-X single-polarization StripMap operational beams used for the generation of the global DEM. These beams are identified as: $[\text{tandem\_a1\_000}, \ldots, \text{tandem\_a1\_090}]$ for the overlapping acquisitions of the first global coverage (from near to far range) and $[\text{tandem\_a2\_005}, \ldots, \text{tandem\_a2\_095}]$ for the second one [55]. These two sets of beams were designed to be mutually displaced of about half beam width, in order to keep a homogeneous performance in the final DEM after the combination of multiple overlapping acquisitions.

We derived the fitting coefficients for the TSX and TDX satellites, separately, as presented in Table I. The estimated $\hat{\sigma}^n(\theta)$ are depicted in Fig. 2, together with the corresponding theoretical noise profiles (dashed black curves) and the averaged noise profiles, derived from the annotated noise fitting coefficients (dashed blue curves) for all considered acquisitions.

The theoretical noise profiles $\sigma^n_{\text{theo}}(\theta)$ are derived as [4]

$$\sigma^n_{\text{theo}}(\theta) = \frac{4^4 \cdot \pi^3 \cdot r^3 \cdot v \cdot \sin\theta \cdot k \cdot T \cdot B_{\text{rg}} \cdot F \cdot L_{\text{at}} \cdot L_{\text{sy}} \cdot L_{\text{az}}}{P_{\text{Tx}} \cdot G_{\text{Tx}} \cdot G_{\text{Rx}} \cdot \lambda^3 \cdot c \cdot \tau_{\text{p}} \cdot PRF} \quad (12)$$

where v is the satellite velocity, k is the Boltzmann constant, T is the receiver temperature, B_{rg} is the bandwidth of the radar pulse, F is the noise figure, L_{sy} denotes the system losses, L_{at} denotes the atmospheric losses, P_{Tx} is the transmit power, G_{Tx} and G_{Rx} are the gains of the transmit and receive antennas, respectively, c is the velocity of light, τ_{p} is the chirp pulse duration, and PRF is the pulse repetition frequency. For the practical evaluation of $\sigma^n_{\text{theo}}(\theta)$, we utilized theoretical values and antenna patterns as defined during the mission design phase [4].

Regarding the noise profiles $\sigma^n_{\text{annot}}(\theta)$ derived from the TanDEM-X product annotation, a set of polynomial coefficients is estimated from receive-only data, which is directly converted to noise power within the processing chain by the operational

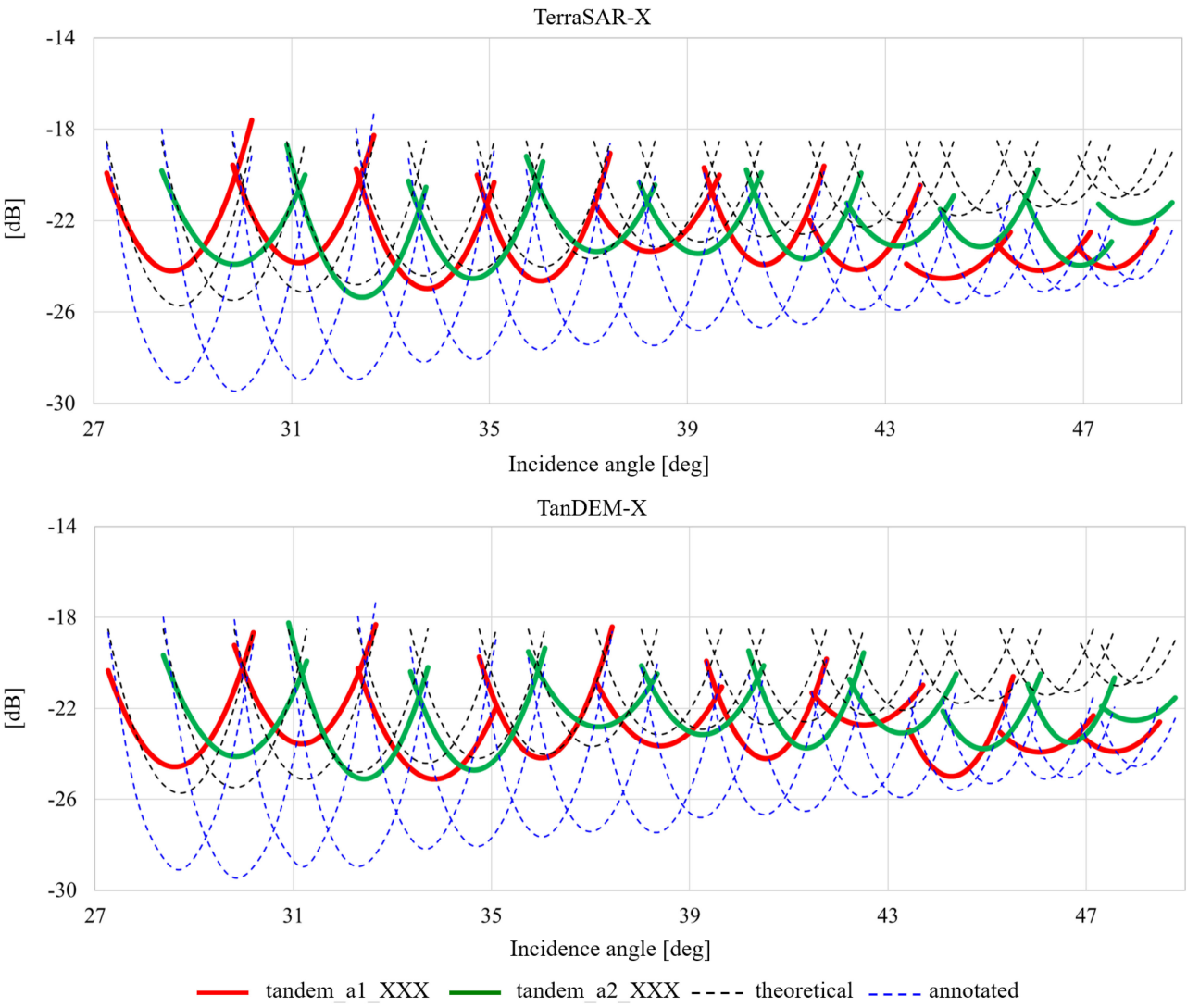

Fig. 2. Estimated noise equivalent sigma naught ($\hat{\sigma}^n(\theta)$) range profiles for all TanDEM-X operational StripMap beams used for the generation of the global DEM, acquired in single-polarization (HH) and with 100-MHz range bandwidth, derived from the second-order polynomial fitting in (11). The profiles are estimated for the TerraSAR-X (top) and the TanDEM-X (bottom) satellites, separately. From left to right: [tandem_a1_000, tandem_a1_$\cdots$, tandem_a1_090] (red) and [tandem_a2_005, tandem_a2_$\cdots$, tandem_a2_095] (green). Corresponding theoretical (dashed black) and annotated (dashed blue) noise equivalent sigma naught profiles.

TanDEM-X processor. These coefficients are included in the Level-1b product annotation and they can be used for retrieving a noise profile in range as presented in [51]. From Fig. 2, one can notice an overall good agreement between the estimated $\hat{\sigma}^n(\theta)$ and the theoretical $\sigma^n_{\text{theo}}(\theta)$ profiles, with $\hat{\sigma}^n(\theta)$ showing a better performance at far range between 2 and 4 dB. On the other hand, considerable offsets in the order of several decibel are visible with respect to the annotated $\sigma^n_{\text{annot}}(\theta)$, especially at near range, where offsets of up to about 8 dB are observed. Their origin was unfortunately not adequately investigated at the beginning of the mission, given other more urgent priorities so that these offsets have not been operationally compensated in the distributed CoSSCs products. Moreover, a good agreement can be seen between both TSX and TDX satellites, which show a similar performance for all beams. On the basis of these findings, we strongly suggest the users to rely on the polynomial profiles that we directly derived from the real data for the computation of $\hat{\sigma}^n(\theta)$ profiles.

Finally, by properly sampling the estimated $\hat{\sigma}^n(\theta)$ profiles in the slant-range direction and by replicating them in the azimuth one, we can obtain a 2-D image of the noise equivalent sigma naught with the same size of the original SAR image for both the master and slave acquisitions, which can be used according to (7) and (10) for the estimation of the SNR decorrelation factor $\hat{\gamma}_{\text{SNR}}$ as in (4).

For the present analysis, we considered TanDEM-X images acquired in bistatic StripMap single-polarization mode (HH channel), since, on the one hand, this is the operational acquisition mode, and on the other hand, the quantization analysis presented later on in Section III could be performed on this kind of data only. In addition, only few TanDEM-X StripMap single-polarization acquisitions in VV channel, as well as

TABLE II
MAXIMUM (MAX), MINIMUM (MIN), AND AVERAGE (MEAN) VALUES OF σ^0 (IN DB) RECORDED OVER CALM WATER SURFACES FOR TANDEM-X STRIPMAP DUAL-POLARIZATION DATA, ACQUIRED AT NEAR, MID, AND FAR RANGE, RESPECTIVELY

StripMap dual-polarization (HH/VV) - HH channel						
Range	Near		Mid		Far	
Beam	StripNear_003		StripNear_008		StripFar_014	
Incidence	[19.87° - 21.66°]		[31.89° - 33.38°]		[44.28° - 45.41°]	
Sensor	TSX	TDX	TSX	TDX	TSX	TDX
Max	-21.48	-21.22	-20.06	-19.49	-18.67	-18.67
Min	-24.97	-24.93	-22.30	-21.72	-20.75	-20.60
Mean	-23.19	-23.13	-21.47	-20.94	-20.06	-19.96

StripMap dual-polarization (HH/VV) - VV channel						
Range	Near		Mid		Far	
Beam	StripNear_003		StripNear_008		StripFar_014	
Incidence	[19.87° - 21.66°]		[31.89° - 33.38°]		[44.28° - 45.41°]	
Sensor	TSX	TDX	TSX	TDX	TSX	TDX
Max	-20.09	-19.86	-20.35	-19.73	-18.86	-18.72
Min	-23.46	-23.29	-22.87	-21.93	-20.51	-20.13
Mean	-21.53	-21.35	-21.84	-21.16	-20.05	-19.67

HH (top) and VV (bottom) channels are separately analyzed, as well as TSX and TDX satellites.

dual-polarization (HH-VV) data-takes, are available so that an assessment of the system noise floor for all dual-polarization beams would not be feasible. Nevertheless, since many users utilize dual-polarization (HH/VV) TanDEM-X data for scientific applications, we performed a dedicated analysis that could help extending this work in such a case. We analyzed three bistatic StripMap dual-polarization data-takes, acquired with beams at near, mid, and far range, respectively. For each polarization channel and satellite, we computed the maximum, minimum, and average σ^0 over calm water surfaces. The results are reported in Table II. These values could be useful to eventually adjust the annotated noise profiles to a more correct absolute level.

III. QUANTIZATION DECORRELATION FACTOR

SAR raw data quantization is performed on board of both TSX and TDX satellites through a lossy BAQ [49]. After digitization of the recorded analog signal (i.e., sampling and quantization using 8 bits/sample), the input signal is quantized utilizing a lower number of bits (typically 2–4 bits/sample). The quantization decision levels are defined depending on the statistics of a considered block of samples. The quantization decorrelation factor γ_{Quant} represents the coherence loss caused by the quantization of the raw data signal and its magnitude strongly depends on the local statistics of the radar backscatter, as well as on the BAQ quantization rate [7].

To estimate $\hat{\gamma}_{\text{Quant}}$, we first consider a bistatic TanDEM-X acquisition where the signals acquired by both the master and slave sensors are commanded with maximum quantization resolution at 8 bits/sample (BAQ bypass). We then requantize the same raw data on ground with the available BAQ rates at 2, 3, and 4 bits/sample. By comparing the coherence map derived from the bypass data $\hat{\gamma}_{\text{Bypass}}$ with the one computed for a certain BAQ rate $\hat{\gamma}_{\text{BAQ}}$, it is possible to precisely retrieve $\hat{\gamma}_{\text{Quant}}$ with respect to the scene characteristics and the quantization rate itself as

$$\hat{\gamma}_{\text{Quant}} = \frac{\hat{\gamma}_{\text{BAQ}}}{\hat{\gamma}_{\text{Bypass}}}. \tag{13}$$

It has been previously demonstrated in [7] and [56] that the coherence loss due to quantization is highly correlated to the local statistics of SAR backscatter, resulting in a larger coherence loss for heterogeneous areas, like urban settlements or mountainous terrain, and in a lower one for more homogeneous areas such as forests, deserts, flat ice, and snow-covered surfaces. Additionally, for a given backscatter distribution, stronger targets are less affected by quantization errors than weaker ones because of a well-known *masking* effect caused by the adaptive quantizer itself [7]. Therefore, both the local mean backscatter β^0_{local} and its spatial standard deviation σ_{local} represent key parameters for the evaluation of the coherence loss for different BAQ rates and they need to be properly estimated from the data. To do so, for each pixel coordinate in the considered single-look complex image, β^0_{local} is evaluated as the expected value of the measured radar brightness, computed within a boxcar window centered around the considered pixel. This allows for mitigating the impact of speckle noise. In this article, we utilize a window of 11×11 pixels, which is the same one used for the coherence estimation in TanDEM-X operational products. Moreover, as presented in [56], each sample in the raw data signal is influenced by all the surrounding scatterers located within an area A of size

$$A = [L_{\text{chirp}} \times L_{\text{s}}] \tag{14}$$

in range and azimuth dimensions, respectively, where L_{chirp} is the chirp length and L_{s} is the radar synthetic aperture. These are defined as

$$L_{\text{chirp}} = \frac{c \cdot D_{\text{c}}}{2 \cdot PRF} \tag{15}$$

$$L_{\text{s}} = \frac{\lambda \cdot h_{\text{sat}}}{L_{\text{a}} \cdot \cos\theta} \tag{16}$$

where D_{c} is the duty cycle, h_{sat} the satellite orbit height, and L_{a} the physical antenna length in azimuth. Given all these considerations, for each pixel σ_{local} is computed as the radar brightness standard deviation in linear unit within a surrounding window of area A (it is then converted in decibel units for visualization purposes). In a nominal StripMap TanDEM-X scenario, A extends by about $[4 \times 7]$ km^2, corresponding to about $[2100 \times 5400]$ pixels in range and azimuth dimensions, respectively.[2] An example of local backscatter statistics is presented in Fig. 3, which depicts the maps of the local backscatter β^0_{local} [see Fig. 3(a)] and the local standard deviation σ_{local} [see Fig. 3(b)], respectively, for an area characterized by the presence of urban settlements, mountainous terrain, and vegetated areas. The effects of using a wide window such as A for the computation of σ_{local} are clearly visible in the corresponding

[2]We assume $D_{\text{c}} = 0.18$, $\lambda = 3.1$ cm for X band, $h_{\text{sat}} \approx 511$ km at the equator, and $L_{\text{a}} = 4.8$ m. The resulting pixel spacing is $D_{\text{rg}} = 1.36$ m in slant range (given a range bandwidth of 100 MHz) and $D_{\text{az}} \approx 2$ m in azimuth. D_{az} might slightly vary depending on the specific acquisition since $D_{\text{az}} = v_{\text{sat}}/PRF$, being $v_{\text{sat}} \approx 7.6$ km/s the sensor velocity, while the PRF changes depending on the specific data-take (exemplary values are shown in Table III).

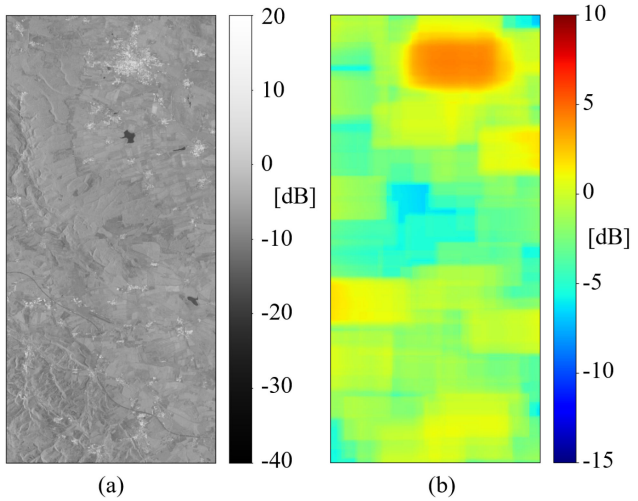

Fig. 3. Example of local backscatter statistics. (a) Local mean backscatter β^0_{local}. (b) Local standard deviation σ_{local}.

image, which appears strongly smoothed. As expected, a higher variability is measured in correspondence of the urban area at the top of the image and in the surrounding regions. This effect is also visible at the bottom of the image, in the presence of high-relief topography.

To model the coherence degradation caused by quantization, we first divide the overall dynamic range of σ_{local} into intervals of 5-dB span, which can be associated with a specific heterogeneity degree of the underlying scene. The 5-dB span was empirically selected as a good compromise between estimation accuracy and overall availability of TanDEM-X data. Afterwards, for each σ_{local} interval, we sample the corresponding β^0_{local} total span into N subintervals of 0.005 dB, and for each subinterval, we compute the mean value of all available coherence degradation measurements, derived as

$$\hat{\gamma}_{\text{Degr}} = (1 - \hat{\gamma}_{\text{Quant}}) \cdot 100. \tag{17}$$

We then model the coherence loss (in percentage unit) caused by quantization as an exponential function, which depends on β^0_{local} (expressed in decibel units)

$$\hat{\gamma}_{\text{Fit}} = \rho_0 \cdot \exp\left(-\rho_1 \cdot \beta^0_{\text{local}}\right) + \rho_2 \tag{18}$$

where $\rho = [\rho_0, \rho_1, \rho_2]$ is a vector of fitting coefficients, which is estimated through a weighted least-squares optimization as

$$\rho = \arg\min_{\rho} ||w \cdot (\hat{\gamma}_{\text{Degr}} - \hat{\gamma}_{\text{Fit}})||^2. \tag{19}$$

Here, w is a vector of weights that are directly proportional to the number of $\hat{\gamma}_{\text{Degr}}$ measurements for each β^0_{local} subinterval and are normalized to the total number of available β^0_{local} measurements.

Finally, the estimate of the quantization decorrelation factor $\hat{\gamma}_{\text{Quant}}$ is derived as

$$\hat{\gamma}_{\text{Quant}} = 1 - \frac{\hat{\gamma}_{\text{Fit}}}{100}. \tag{20}$$

For the current analysis, we have analyzed ten experimental TanDEM-X acquisitions specifically commanded with BAQ bypass (i.e., 8 bits/sample) over selected test sites, characterized by different land cover types, and therefore, various local backscatter statistics. All test sites and the corresponding main acquisition parameters (θ and PRF) are listed in Table III. For each image, we utilize an area corresponding to 60% of the total extension for the derivation of the coherence loss models for different BAQ rates and the remaining 40% for the verification of the proposed method.[3]

TABLE III
TEST SITES USED FOR THE QUANTIZATION ANALYSIS, TOGETHER WITH THE CORRESPONDING PREDOMINANT LAND COVER, THE INCIDENCE ANGLE θ, AND THE COMMANDED PRF

Test site	Land cover	θ [°]	PRF [Hz]
Amazon Forest (BRA)	Homogeneous rainforest	44.5	3562
Antarctica	Snow and i e with topography	36.2	3356
Greenland	Snow and ice, flat	40.6	3724
Death Valley (USA)	Soil and rocks, mountainous	40.6	3752
Mexico City	Urban area, mountainous	33.6	3854
Malaysia	Tropical forest, mountainous	47.6	3807
Las Vegas (USA)	Urban area, flat	36.1	3724
Rondônia (BRA)	Rainforest with clear-cuts	29.8	3688
Iowa (USA)	Agricultural area, flat	33.8	3554
Naples (ITA)	Urban/agricultural area with topography	36.9	3461

An example of resulting fitting curves is depicted in Fig. 4 for a BAQ setting of 2 bits/sample for both the master and slave acquisitions, considering the following σ_{local} intervals: $\sigma_{\text{local}} \in [-15\text{ dB}, -10\text{ dB}]$, $\sigma_{\text{local}} \in [-10\text{ dB}, -5\text{ dB}]$, and $\sigma_{\text{local}} \in [5\text{ dB}, 10\text{ dB}]$. The resulting fitting curves for all σ_{local} intervals are depicted in Fig. 5. BAQ settings of 4, 3, and 2 bits/sample, applied to both the master and slave acquisitions, are considered. One can clearly notice a lower degradation in the presence of homogeneous areas, characterized by lower σ_{local}, as well as for higher β^0_{local} levels. As expected, the coherence degradation significantly increases with a higher BAQ quantization rate (e.g., 2 bits/sample). For example, for homogeneous areas ($\sigma_{\text{local}} < -10$ dB), one can expect a coherence degradation below 3% for a BAQ rate of 4 bits/sample, while this can increase up to about 20% if 2 bits/sample are used. The degradation remains below 20% over highly heterogeneous areas ($\sigma_{\text{local}} > 5$ dB) for 4 bits/sample, while, when considering 2 bits/sample, it reaches considerable values especially for low backscatter levels. As previously mentioned, for highly heterogeneous areas, a higher coherence loss is also caused by a sort of masking effect, also called *low-scatterer suppression* effect, which degrades the reconstruction quality of low-amplitude targets, as extensively discussed in work presented in [7].

The resulting set of exponential fitting coefficients for all the considered BAQ quantization rates is listed in Table IV, separately derived for different ranges of σ_{local}. The reader should be aware that the fitted models are typically considered to be reliable only within the backscatter statistics intervals where real TanDEM-X measurements were available. This information is also provided in Table IV for both β^0_{local} and σ_{local} (validity intervals). Moreover, for the practical application of the proposed fitting coefficients in the rare cases in which the measured σ_{local} values are outside the considered intervals, we

[3]For the acquisition over Naples, Italy, we considered only the portion of the image acquired over land (about 50%), avoiding the Mediterranean Sea.

TABLE IV
EXPONENTIAL FITTING COEFFICIENTS USED FOR THE COMPUTATION OF $\hat{\gamma}_{\text{Fit}}$ WITH RESPECT TO THE BYPASS CASE, REFERRING TO THE EXPONENTIAL MODEL IN (19) AND CORRESPONDING TO BAQ SETTINGS OF 2, 3, AND 4 BITS/SAMPLE FOR BOTH THE MASTER AND SLAVE SENSORS

Validity Intervals	σ_{local} [dB] / β^0_{local} [dB]	[-15, -10] / [-21, -3]	[-10, -5] / [-21.3, 2.6]	[-5, 0] / [-21.5, 3.7]	[0, 5] / [-18.5, 9.3]	[5, 10] / [-18.9, 9.4]
BAQ: 2 bits/sample	ρ_0	16.9139	0.784	1.6957	4.6866	10.4185
	ρ_1	0.0443	0.186	0.1695	0.1311	0.116
	ρ_2	-20.9125	3.3794	3.4641	3.1782	0.0844
BAQ: 3 bits/sample	ρ_0	6.7994	0.1787	0.3926	0.8698	2.3587
	ρ_1	0.0392	0.2093	0.2018	0.1815	0.1677
	ρ_2	-8.4396	1.1697	1.1607	1.8951	1.1276
BAQ: 4 bits/sample	ρ_0	1.2327	0.0513	0.1334	0.2214	0.6027
	ρ_1	0.056	0.2174	0.2021	0.1945	0.1941
	ρ_2	-1.6657	0.3816	0.3233	0.6696	0.531

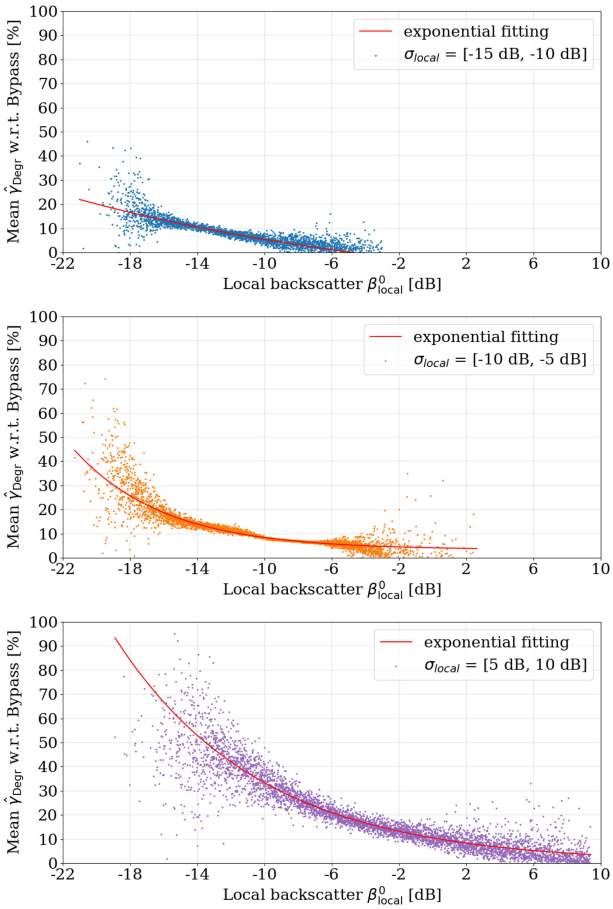

Fig. 4. Measured coherence degradation $\hat{\gamma}_{\text{Degr}}$ with respect to the bypass case as a function of β^0_{local} and for exemplary σ_{local} intervals (from top to bottom: (blue dots) $\sigma_{\text{local}} \in [-15\text{ dB}, -10\text{ dB}]$, (orange dots) $\sigma_{\text{local}} \in [-10\text{ dB}, -5\text{ dB}]$, and (violet dots) $\sigma_{\text{local}} \in [5\text{ dB}, 10\text{ dB}]$). Exponential fitting curves $\hat{\gamma}_{\text{Fit}}$ (red). All plot correspond to a BAQ setting of 2 bits/sample for both the master and slave channels.

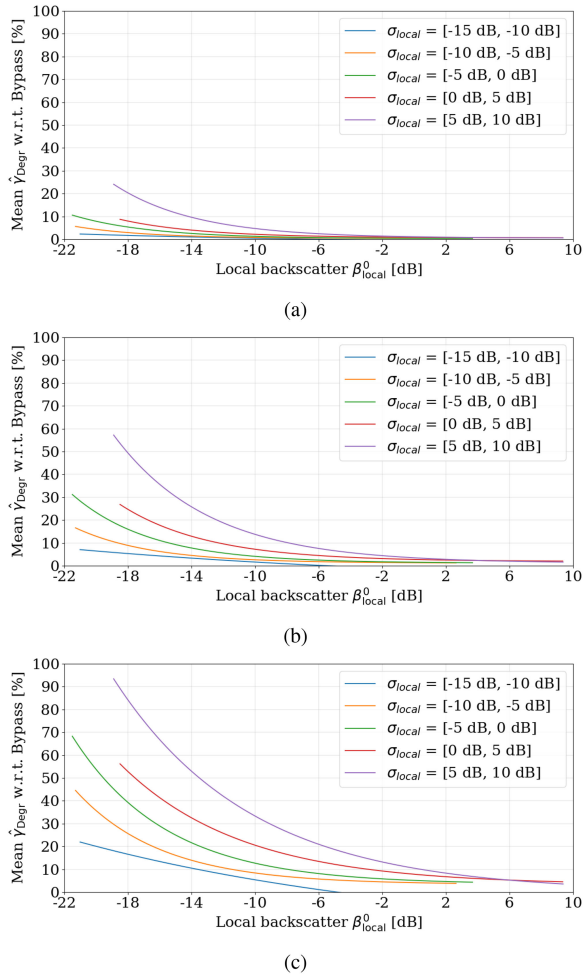

Fig. 5. Exponential fitting curves used for estimating $\hat{\gamma}_{\text{Degr}}$ with respect to the BAQ bypass case as a function of β^0_{local} and for different σ_{local} intervals. Each plot corresponds to a different BAQ setting for both the master and slave sensors. (a) 4 bits/sample. (b) 3 bits/sample. (c) 2 bits/sample.

assume that, if $\sigma_{\text{local}} < 15$ dB, then the coherence degradation is negligible, while if $\sigma_{\text{local}} > 10$ dB, it can be approximated using the $\sigma_{\text{local}} \in [5\text{ dB}, 10\text{ dB}]$ curves.

Finally, the reliability of the derived fitting coefficients has been evaluated over the remaining portions of all the considered images (40% of the pixels), which were not utilized for the derivation of the fitting coefficients in Table IV. An example of validation over the Rond ô nia, Brazil, test site is depicted in Fig. 6, where three different BAQ rates are considered (2, 3, and 4 bits/sample). The red curves represent the ratio between $\hat{\gamma}_{\text{BAQ}}$ and $\hat{\gamma}_{\text{Bypass}}$ [i.e., $\hat{\gamma}_{\text{Quant}}$, as in (13)], while the blue curves identify the ratio $\hat{\gamma}_{\text{Comp}}/\hat{\gamma}_{\text{Bypass}}$, where $\hat{\gamma}_{\text{Comp}}$ is the reconstructed

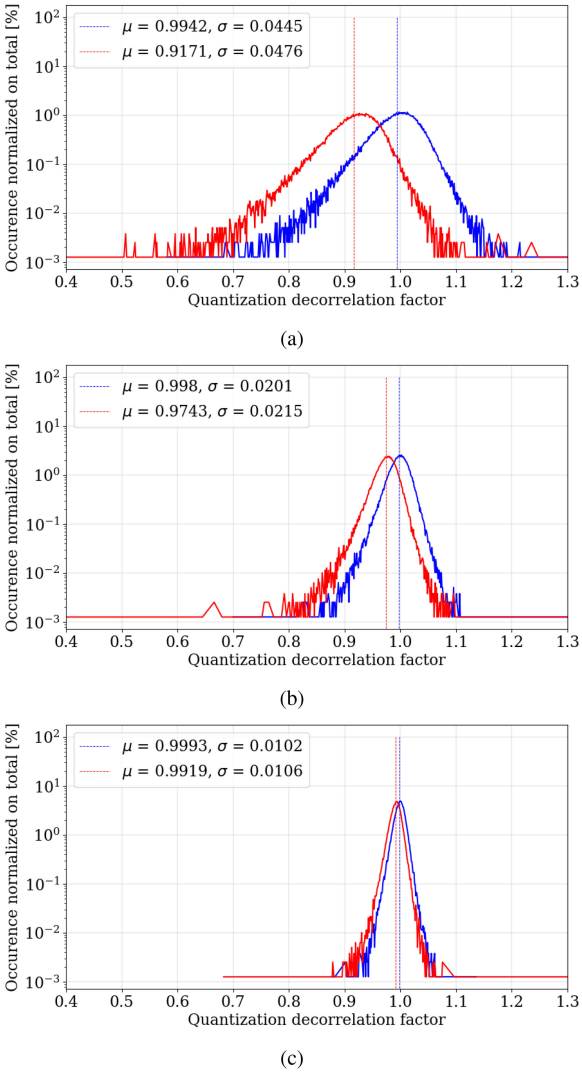

Fig. 6. Verification of the derived exponential fitting curves, considering the Rond ô nia (BRA) test site, quantized using, from top to bottom: (a) 2, (b) 3, and (c) 4 bits/sample. The distributions represent $\hat{\gamma}_{\text{Quant}}$ (red), and the ratio between the reconstructed coherence $\hat{\gamma}_{\text{Comp}}$ and the original $\hat{\gamma}_{\text{Bypass}}$ (blue). μ and σ indicate the distribution mean value and standard deviation, respectively.

coherence after compensating for the estimated $\hat{\gamma}_{\text{Quant}}$ as

$$\hat{\gamma}_{\text{Comp}} = \frac{\hat{\gamma}_{\text{Tot}}}{\hat{\gamma}_{\text{Quant}}}. \tag{21}$$

μ and σ represent the mean value and standard deviation of the $\hat{\gamma}_{\text{Quant}}$ distribution (before compensation) and of the ratio between the reconstructed $\hat{\gamma}_{\text{Comp}}$ and the original $\hat{\gamma}_{\text{Bypass}}$ (after compensation), respectively. For the validation, we considered input pixels characterized by a coherence higher than 0.3 only, in order to avoid the use of measurements with no informative content since already completely decorrelated. If an ideal compensation for γ_{Quant} could be applied, the blue curve would shrink to a constant value equal to one, meaning that the original bypass coherence would be perfectly reconstructed from the quantized one. In a real case scenario, a remaining dispersion of the error is expected. Nevertheless, the validity of the proposed methodology is confirmed by the mean values μ of the blue curves. They approximate the unit for all different test sites, which means that, on average, the bypass coherence is correctly reconstructed by compensating for the estimated $\hat{\gamma}_{\text{Quant}}$. It is worth noting thatthe different impact of the BAQ rate on $\hat{\gamma}_{\text{Quant}}$, which reaches about 10% on average ($\simeq 0.9$) for 2 bits/sample, while it is almost negligible for 4 bits/sample (about 1%).

The overall performance for all considered test sites is summarized in Table V, which presents the mean values μ and standard deviations σ before and after $\hat{\gamma}_{\text{Quant}}$ compensation. As it can be seen, in all cases, μ after compensation well approximates the unit for all different types of land cover and BAQ quantization rates. This confirms the validity of the proposed exponential models [i.e., $\hat{\gamma}_{\text{Fit}}$ in (19)].

Moreover, some additional aspects have to be considered regarding the practical estimation of σ_{local}. As mentioned before, it is computed within a boxcar window of area A as in (14). Clearly, the full estimation window around pixels located in the vicinity of the image borders is not available. This could result in the selection of a wrong fitting function in Table IV, due to an imprecise estimation of σ_{local}. We have assessed this effect in a worst case scenario, where $\hat{\gamma}_{\text{Quant}}$ is estimated at the corners of the image, considering, therefore, a boxcar window of size $A_{\text{worst}} = [L_{\text{chirp}}/2 \times L_{\text{s}}/2]$. When applying this modified window to the ten images used for the analysis (in order to be as much scene-independent as possible), and considering a BAQ rate of 3 bits/sample, a wrong fitting function has been selected in about 17.8% of the cases, resulting in an overall expected error in the coherence loss estimation of less than 1%. Therefore, it can be reasonably assumed that a reduced window size can be utilized for pixels close to the image borders without a significant decrease of the estimation performance.

Finally, as already mentioned for the estimation of the SNR decorrelation factor in Section II, the reader should be aware that the present results were obtained by considering TanDEM-X data acquired in single horizontal (HH) polarization only. A similar analysis could not be performed on either single vertical (VV) polarization channel or dual-polarization (HH-VV) data-takes since only very few of them have been acquired up to now using BAQ bypass (8 bits/sample). Nevertheless, we expect the derived fitting coefficients in Table IV to be valid also for other polarization channels, since in principle, the same BAQ compression algorithm is applied. Clearly, different backscatter statistics could be observed at different polarizations, depending on the type of the specific backscattering mechanism. This might lead to the use of different fitting coefficients for the same illuminated area on ground. Moreover, the size A of the window required for the computation of σ_{local} also varies depending on the acquisition parameters, as described in (15) and (16).

IV. Other Sources of Decorrelation

Regarding all other decorrelation sources to be compensated for the estimation of $\hat{\gamma}_{\text{Vol}}$, which are expressed through the remaining decorrelation factors in (6), we assume that the theoretical computations and assumptions on the TanDEM-X system presented in [4] still hold. Therefore, for TanDEM-X StripMap acquisitions, range and azimuth ambiguities can be expected to contribute to a decorrelation factor $\gamma_{\text{Amb}} > 0.97$, which varies depending on the specific beam. Common-bandwidth range

TABLE V
ACCURACY ANALYSIS OF THE DERIVED EXPONENTIAL FITTING COEFFICIENTS FOR THE ESTIMATION OF $\hat{\gamma}_{\mathrm{Fit}}$, APPLIED TO DIFFERENT TYPES OF LAND COVERS

Test site	Before compensation						After compensation					
	BAQ: 2 bits/sample		BAQ: 3 bits/sample		BAQ: 4 bits/sample		BAQ: 2 bits/sample		BAQ: 3 bits/sample		BAQ: 4 bits/sample	
	μ	σ	μ	σ	μ	σ	μ	σ	μ	σ	μ	σ
Amazon Forest (BRA)	0.916	0.1184	0.9739	0.0229	0.992	0.0118	0.9934	0.1288	0.998	0.0236	0.9996	0.0119
Antarctica	0.8846	0.1043	0.9585	0.0542	0.9864	0.0288	1.0073	0.1731	1.0003	0.0543	1	0.0284
Greenland	0.9293	0.0293	0.9779	0.0152	0.993	0.0083	1.0024	0.0313	1.0005	0.0155	1.0002	0.0084
Death Valley (USA)	0.8779	0.0994	0.9583	0.0429	0.9864	0.0216	0.9957	0.1283	0.9986	0.0406	0.999	0.0208
Mexico City	0.8433	0.1088	0.9411	0.056	0.9802	0.0253	1.0089	0.1237	1.001	0.053	0.9998	0.0235
Malaysia	0.8652	0.123	0.9495	0.0619	0.9833	0.0326	1.0167	0.1709	1.0026	0.0642	1.0007	0.0326
Las Vegas (USA)	0.848	0.1425	0.9457	0.0872	0.9854	0.0721	1.0185	0.1857	1.0075	0.093	1.0052	0.0746
Rondônia (BRA)	0.9171	0.0476	0.9743	0.0215	0.9919	0.0106	0.9942	0.0445	0.998	0.0201	0.9993	0.0102
Iowa (USA)	0.9103	0.0457	0.9727	0.0206	0.991	0.0096	1.0309	0.0592	1.0108	0.0222	1.0031	0.0098
Naples (ITA)	0.8301	0.0903	0.9403	0.0423	0.9801	0.0184	0.9872	0.139	0.994	0.0534	0.9967	0.0205

μ and σ represent the mean value and standard deviation of the $\hat{\gamma}_{\mathrm{Quant}}$ (before compensation) and of the ratio between the reconstructed $\hat{\gamma}_{\mathrm{Comp}}$ and the original $\hat{\gamma}_{\mathrm{Bypass}}$ (after compensation), respectively. An example of such distributions for different BAQ rates is presented in Fig. 6.

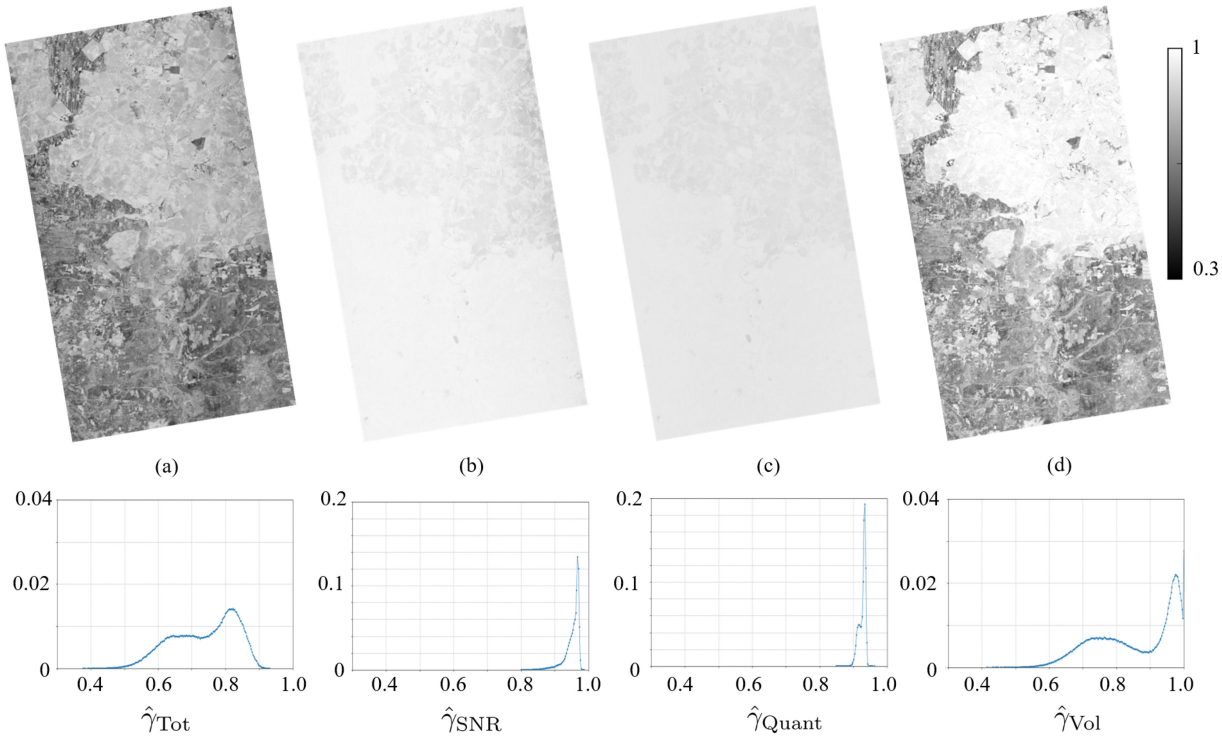

Fig. 7. Example of $\hat{\gamma}_{\mathrm{Vol}}$ estimation. (a) Estimated total interferometric coherence $\hat{\gamma}_{\mathrm{Tot}}$. The estimated (b) SNR decorrelation factor $\hat{\gamma}_{\mathrm{SNR}}$, (c) quantization decorrelation factor $\hat{\gamma}_{\mathrm{Quant}}$, and (d) volume decorrelation factor $\hat{\gamma}_{\mathrm{Vol}}$, for a nominal TanDEM-X bistatic data-take acquired with beam tanDEM_a1_070 and a height of ambiguity of 87 m, using a BAQ quantization rate of 2 bits/sample. The corresponding normalized histograms are depicted below each image.

filtering is operationally performed during focusing and residual misregistration errors in range might result in $\gamma_{\mathrm{Rg}} > 0.98$. A similar decorrelation is expected for residual misregistrations in azimuth and relative shift of the Doppler spectra, leading to $\gamma_{\mathrm{Az}} > 0.98$. The considered values represent a worst-case scenario and will not impact all coherence pixels in the same way. Overall, it is reasonable to quantify all these contributions in a conservative decorrelation factor of about 0.98 all over the image, corresponding to an additional 2% of decorrelation.

V. FINAL PRODUCT AND APPLICATION SCENARIOS

An example of $\hat{\gamma}_{\mathrm{Vol}}$ estimation is presented in Fig. 7, which depicts an area characterized by the presence of both densely vegetated and sparsely or nonvegetated areas. Together with the initial coherence $\hat{\gamma}_{\mathrm{Tot}}$, $\hat{\gamma}_{\mathrm{SNR}}$, $\hat{\gamma}_{\mathrm{Quant}}$, and the derived $\hat{\gamma}_{\mathrm{Vol}}$ are depicted. For each quantity, the corresponding normalized histograms are depicted as well. The considered data-take was acquired using a BAQ quantization rate of 2 bits/sample. In this example, one can notice the slant range dependence of the $\hat{\gamma}_{\mathrm{SNR}}$ shown in Fig. 7(b), which is inversely proportional to the curvature of the noise equivalent sigma naught profiles depicted in Fig. 2. Indeed, the higher level of system noise at the swath's borders (near and far range), mainly caused by a lower antenna pattern gain, results in a more severe SNR decorrelation, while a better coherence is maintained at the beam's center. An overall nonnegligible decorrelation contribution of about 10% is clearly visible in the derived $\hat{\gamma}_{\mathrm{Quant}}$ as well [see Fig. 7(c)]. Moreover,

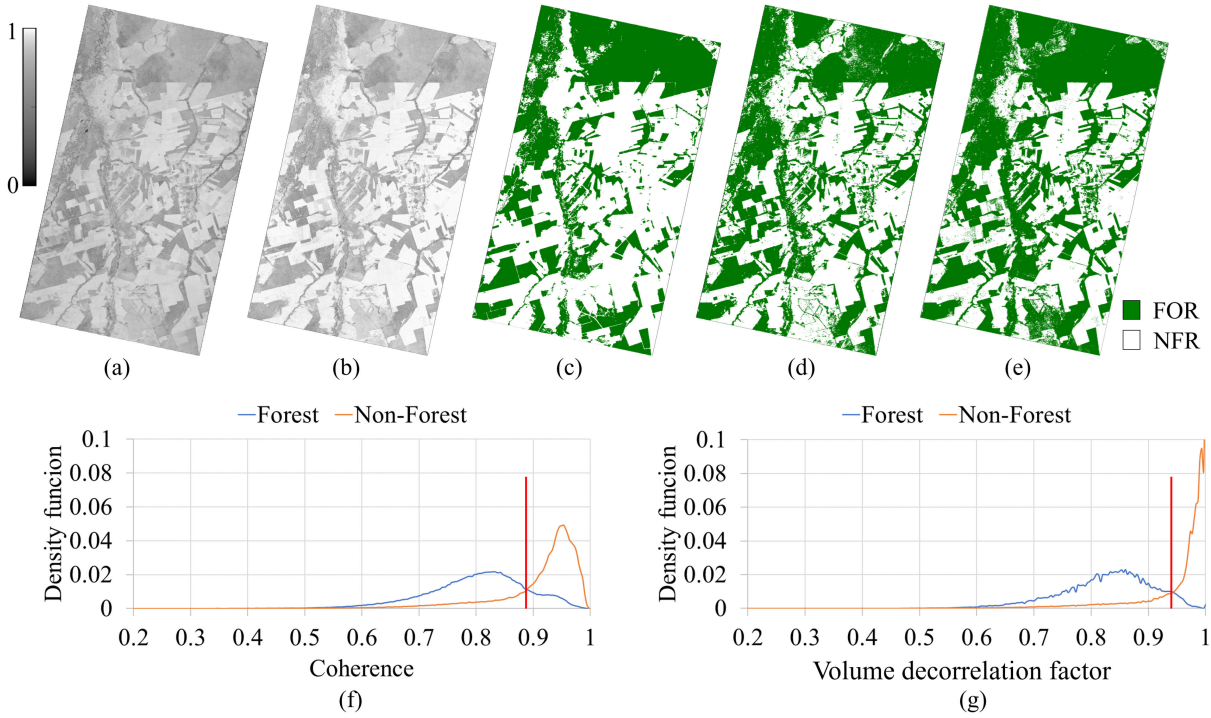

Fig. 8. Example of forest mapping over the Amazon rainforest. (a) TanDEM-X interferometric coherence $\hat{\gamma}_{\text{Tot}}$ image. (b) Derived volume decorrelation factor $\hat{\gamma}_{\text{Vol}}$. (c) Landsat-derived reference forest map as in [42] (Forest (FOR) in green and Non-Forest (NFR) in white). (d) Binary Forest/Non-Forest map derived from (a) by applying the red threshold in (f). (e) Forest/Non-Forest map derived from (b) by applying the red threshold in (g). (f) and (g) Normalized histograms of the coherence (a) and volume decorrelation factor (b), respectively, for the classes Forest and Non-Forest, derived by applying the reference map in (c). The vertical red lines identify the crossing value between the two distributions.

it can be seen how the distribution of $\hat{\gamma}_{\text{Vol}}$ is skewed toward the unit and characterized by a clearer bimodal shape, with respect to the initial $\hat{\gamma}_{\text{Tot}}$. This clearly identifies the presence of two main kinds of scattering mechanisms characterizing vegetated ares, which appear darker in the $\hat{\gamma}_{\text{Vol}}$ image, and nonvegetated, highly coherent ones.

Finally, as practical application examples of the difference between using the newly derived $\hat{\gamma}_{\text{Vol}}$ and the total interferometric coherence $\hat{\gamma}_{\text{Vol}}$, we consider now two different scenarios, concerning forest mapping and forest height estimation.

TABLE VI
CONFUSION MATRICES FOR THE FOREST MAPPING EXAMPLE INTRODUCED IN FIG. 8 (FOR = FOREST, NFR = NON-FOREST)

Prediction \ True class	FOR	NFR
FOR	35.41%	10.38%
NFR	7.48%	46.73%

(a)

Prediction \ True class	FOR	NFR
FOR	39.42%	9.09%
NFR	3.47%	48.02%

(b)

(a) Classification based on the interferometric coherence in Fig. 8(d). (b) Classification based on the volume decorrelation factor in Fig. 8(e). The prediction performance is evaluated with respect to the Landsat-derived forest map (true class) in Fig. 8(c).

A. Forest Mapping

We consider an area located in the Amazon rainforest, as depicted in Fig. 8. Fig. 8(a) and (b) depicts the TanDEM-X interferometric coherence $\hat{\gamma}_{\text{Tot}}$ and the derived volume decorrelation factor $\hat{\gamma}_{\text{Vol}}$, respectively, while Fig. 8(c)–(e) shows three binary Forest/Non-Forest maps over the same area, derived from Landsat optical data as in [42] [see Fig. 8(c)] and by applying a decision threshold to the interferometric coherence [see Fig. 8(d)] and to the volume decorrelation factor [see Fig. 8(e)], respectively. The considered thresholds correspond to the vertical red lines in Fig. 8(f) and (g) and identify the crossing value between the distributions of both Forest and Non-Forest classes, derived from the interferometric coherence and volume decorrelation factor, respectively. Such histograms have been derived using as reference the binary forest map derived from Landsat [see Fig. 8(c)]. One can notice how the distribution of the Non-Forest class from the volume decorrelation factor is significantly skewed to the right with respect to the one derived from the coherence. This is expected, since negligible volume scattering effects occur in the presence of bare soil. Moreover, this also allows for a better separation between the distributions of the two land cover classes, resulting in an improved classification performance, which is documented in the confusion matrices in Table VI (a) and (b). In particular, the occurrence of misclassifications significantly decreases, going from 17.86% down to 12.56%.

B. Forest Height Estimation

We now consider an application scenario for the retrieval of forest canopy height from single-polarization TanDEM-X StripMap data. A state-of-the-art algorithm for the estimation

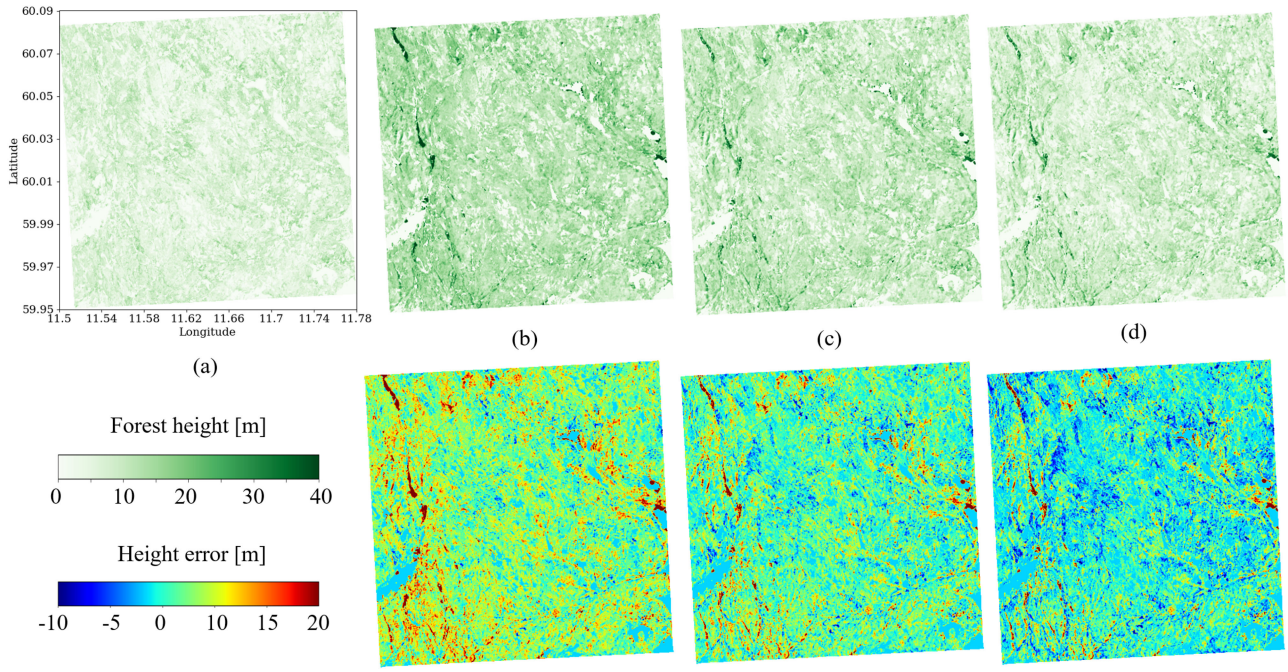

Fig. 9. Example of forest height estimation from TanDEM-X single-polarization data from the inversion of the simplified RVoG model in (24). (a) Reference Lidar CHM model. (Top) Estimated forest height and (bottom) height error derived using as (b) input $\hat{\gamma}_{\text{Tot}}$, (c) $\hat{\gamma}_{\text{Tot}}/\hat{\gamma}_{\text{SNR}}$, and (d) $\hat{\gamma}_{\text{Vol}}$. Invalid pixels and values lower than 1 m in the Lidar data are displayed in white in the forest height maps and are set to zero in the height error maps.

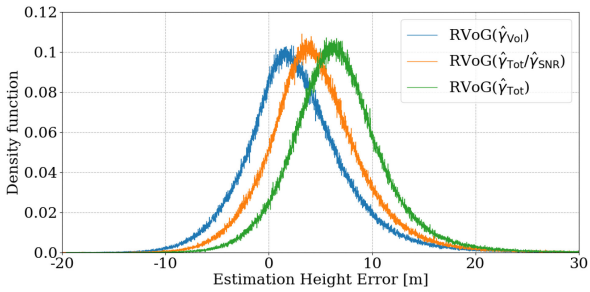

Fig. 10. Histograms of the forest height estimation error with respect to the reference Lidar CHM, derived using as input $\hat{\gamma}_{\text{Tot}}$ (green), $\hat{\gamma}_{\text{Tot}}/\hat{\gamma}_{\text{SNR}}$ (orange), and $\hat{\gamma}_{\text{Vol}}$ (blue).

of tree height using polarimetric SAR interferometry relies on the inversion of the random volume over ground (RVoG) model, presented in [9]. It describes a two-layer model composed by a volumetric layer with randomly oriented scatterers superimposed on a ground layer, which accounts for a direct dihedral scattering contribution

$$\tilde{\gamma}_{\text{Vol}} = \exp\left(ik_{\text{z}}z_0\right)\frac{\tilde{\gamma}_{\text{V}} + m}{1+m}. \tag{22}$$

Here, $\tilde{\gamma}_{\text{Vol}}$ represents the volume decorrelation contribution at a certain polarization, $k_{\text{z}} = (2\pi)/h_{\text{amb}}$ is the vertical wavenumber, z_0 is the reference height at the bottom of the volume, and m represents the ground-to-volume ratio. $\tilde{\gamma}_{\text{V}}$ identifies the decorrelation generated by the volume only and it is typically expressed as an exponential decay, which depends on the canopy height h_{v} and the extinction rate σ_{e}, characterizing the attenuation through the volume. The canopy height can then be retrieved by inverting the model under the assumption that one polarization channel coherence has no ground contribution (i.e., $m = 0$) [10]. Since such a procedure requires the use of full-polarimetric data, the model was simplified for single-polarization data in [12], assuming a known underlying topography derived from a digital terrain model. Since such an information is only seldom available, the work in [28] assumed a fix $\sigma_{\text{e}} = 0$, which holds in case of short wavelengths. If, additionally to the last condition, it is assumed that X-band waves do not penetrate till the ground, the model can be approximated with a sinc function as in [27]–[29]

$$|\tilde{\gamma}_{\text{Vol}}| \simeq \left|\text{sinc}\left(\pi\frac{h_{\text{v}}}{h_{\text{amb}}}\right)\right|. \tag{23}$$

Finally, assuming that $h_{\text{v}} \leq h_{\text{amb}}$, the sinc function can be approximated with a simple linear model as [28]

$$|\tilde{\gamma}_{\text{Vol}}| \simeq \left|1 - \frac{h_{\text{v}}}{h_{\text{amb}}}\right|. \tag{24}$$

This last formulation has already been used in several works in the literature for the estimation of forest height from TanDEM-X single-polarization data (e.g., [28], [31], and [34]). We now consider the simplified model in (24) and its inversion to retrieve h_{v} from a single-polarization TanDEM-X StripMap acquisition in the following three different cases:

1) the total coherence is used as input, having $|\tilde{\gamma}_{\text{Vol}}| = \hat{\gamma}_{\text{Tot}}$;
2) the volume decorrelation component is approximated as $|\tilde{\gamma}_{\text{Vol}}| = \hat{\gamma}_{\text{Tot}}/\hat{\gamma}_{\text{SNR}}$;
3) the estimated volume decorrelation factor is used as input so that $|\tilde{\gamma}_{\text{Vol}}| = \hat{\gamma}_{\text{Vol}}$.

For this purpose, we selected a test site located in Norway and a TanDEM-X bistatic single-polarization data-take, acquired

TABLE VII
FOREST HEIGHT ESTIMATION PERFORMANCE: ROOT MEAN SQUARE ERROR (RMSE), MEAN ABSOLUTE ERROR (MAE), MEAN ERROR (ME), AND ERROR STANDARD DEVIATION (STD)

Input	RMSE	MAE	ME	STD
$\hat{\gamma}_{\mathrm{Tot}}$	8.62m	7.14m	6.9m	5.17m
$\hat{\gamma}_{\mathrm{Tot}}/\hat{\gamma}_{\mathrm{SNR}}$	6.87m	5.35m	4.66m	5.05m
$\hat{\gamma}_{\mathrm{Vol}}$	5.94m	4.32m	2.78m	5.25m

with the $\mathrm{tandem\_a1\_030}$ beam and characterized by $h_{\mathrm{Amb}} = 55$ m. Here, a reference canopy height model (CHM) derived from Lidar data is available for the evaluation of the estimation performance. This reference, depicted in Fig. 9(a), is characterized by an original spatial resolution of about 1 m, which was then multilooked to 12 m for matching the resolution of TanDEM-X data [57]. The resulting forest height maps, obtained from the inversion of (24), for the three considered cases are presented in Fig. 9(b) and (d), together with the corresponding height error maps, computed with respect to the reference Lidar CHM. Invalid pixels and values lower than 1 m in the Lidar data are displayed in white in the forest height maps and set to zero in the height error maps. They are no further considered for the present analysis. The histograms of the estimation height error for the three considered cases are depicted in Fig. 10, while standard performance metrics are summarized in Table VII. The following metrics are considered: root mean square error (RMSE), mean absolute error (MAE), mean error (ME), and error standard deviation (STD). As it can be seen, all models tend to overestimate the height of the forest. The best performance is achieved when the estimated $\hat{\gamma}_{\mathrm{Vol}}$ is used as input to the simplified RVoG model, resulting in the lower offsets, while all three considered input configurations show a comparable behavior in terms of standard deviation of the error.

VI. CONCLUSION

In this article, we presented a detailed analysis of decorrelation sources in TanDEM-X bistatic single-polarization StripMap data, which impact the estimation of the volume decorrelation factor $\hat{\gamma}_{\mathrm{Vol}}$. In particular, we focused on the estimation of the two predominant decorrelation factors: the SNR decorrelation factor $\hat{\gamma}_{\mathrm{SNR}}$ and the quantization decorrelation factor $\hat{\gamma}_{\mathrm{Quant}}$.

Regarding $\hat{\gamma}_{\mathrm{SNR}}$, for each operational TanDEM-X single-polarization (HH) StripMap beam used for the generation of the global DEM, we estimated the corresponding noise equivalent sigma naught profile directly from real SAR data. From this, we derived a set of polynomial coefficients that can be utilized for the precise computation of the image SNR, and consequently, of the SNR decorrelation factor. Moreover, concerning $\hat{\gamma}_{\mathrm{Quant}}$, we performed an extended analysis of the impact of local backscatter statistics and of the quantization rate on the estimated coherence degradation. We then derived a series of LUTs for the retrieval of the quantization decorrelation factor, with respect to the aforementioned parameters. We validated the proposed method and LUTs by considering different land cover scenarios and quantization rates, achieving a satisfactory average performance. Following the procedure proposed in this article, TanDEM-X data users should be able to derive the volume decorrelation factor from the bistatic coherence in a more precise way with respect to current state-of-the-art approximations used in the literature.

In order to confirm these findings, we investigated two basic application scenarios that require the use of $\hat{\gamma}_{\mathrm{Vol}}$: forest mapping and forest height estimation. Here, we implemented two basic approaches, based on a simple thresholding method for the former and on a simplified linear version of the random volume over the ground model for the latter. In both cases, the best performance was achieved when using the estimated $\hat{\gamma}_{\mathrm{Vol}}$ with respect to the total coherence, confirming the necessity for a better estimation of noise sources in TanDEM-X interferometric data. The reader should be aware that the final performance could surely be improved by utilizing more sophisticated techniques rather than the proposed ones also when relying on the coherence only. For example, machine learning-based classifiers or *a posteriori* calibration of the random volume over the ground model would improve the overall results. Nevertheless, this lies beyond the scope of this article and the aim of this basic exercise was to highlight how a better estimation of $\hat{\gamma}_{\mathrm{Vol}}$ surely represents an advantage for many different scenarios. We are convinced that a variety of scientific and technical applications will benefit from a more precise estimation of the volume decorrelation factor, allowing for an accurate modeling of the physics behind volume scattering mechanisms using TanDEM-X bistatic data.

ACKNOWLEDGMENT

The authors would like to thank S. Puliti of the Norwegian Institute of Bioeconomy Research (NIBIO), Norway, for providing the Lidar CHM data, which is part of a public acquisition at national level. The authors would also like to thank the anonymous reviewers for all their valuable comments, which helped improving the content and quality of the manuscript.

REFERENCES

[1] R. Bamler and P. Hartl, "Synthetic aperture radar interferometry," *Inverse Problems*, vol. 14, no. 4, pp. R1–R54, 1998.
[2] R. Touzi, A. Lopes, J. Bruniquel, and P. W. Vachon, "Coherence estimation for SAR imagery," *IEEE Trans. Geosci. Remote Sens.*, vol. 37, no. 1, pp. 135–149, Jan. 1999.
[3] H. Zebker and J. Villasenor, "Decorrelation in interferometric radar echoes," *IEEE Trans. Geosci. Remote Sens.*, vol. 30, no. 5, pp. 950–959, Sep. 1992.
[4] G. Krieger *et al.*, "TanDEM-X: A satellite formation for high-resolution SAR interferometry," *IEEE Trans. Geosci. Remote Sens.*, vol. 45, no. 11, pp. 3317–3341, Oct. 2007.
[5] F. Gatelli, A. M. Guarieri, F. Parizzi, P. Pasquali, C. Prati, and F. Rocca, "The wavenumber shift in SAR interferometry," *IEEE Trans. Geosci. Remote Sens.*, vol. 32, no. 4, pp. 855–865, Jul. 1994.
[6] F. Rocca, "Modeling interferogram stacks," *IEEE Trans. Geosci. Remote Sens.*, vol. 45, no. 10, pp. 3289–3299, Oct. 2007.
[7] M. Martone, B. Bruätigam, and G. Krieger, "Quantization effects in TanDEM-X data," *IEEE Trans. Geosci. Remote Sens.*, vol. 53, no. 2, pp. 583–597, Jun. 2014.
[8] M. Martone, P. Rizzoli, and G. Krieger, "Volume decorrelation effects in TanDEM-X interferometric SAR data," *IEEE Geosci. Remote Sens. Lett.*, vol. 13, no. 12, pp. 1812–1816, Oct. 2016.

[9] K. P. Papathanassiou and S. R. Cloude, "Single-baseline polarimetric SAR interferometry," *IEEE Trans. Geosci. Remote Sens.*, vol. 39, no. 11, pp. 2352–2363, Nov. 2001.

[10] S. R. Cloude and K. Papathanassiou, "Three-stage inversion process for polarimetric SAR interferometry," *IEE Proc.—Radar, Sonar Navigat.*, vol. 150, no. 3, pp. 125–134, Jun. 2003.

[11] S. R. Cloude, "Polarization coherence tomography," *Radio Sci.*, vol. 41, pp. 1–27, Aug. 2006.

[12] F. Kugler, S.-K. Lee, I. Hajnsek, and K. Papathanassiou, "Forest height estimation by means of Pol-InSAR data inversion: The role of the vertical wavenumber," *IEEE Trans. Geosci. Remote Sens.*, vol. 53, no. 10, pp. 5294–5311, Oct. 2014.

[13] J. E. S. Fransson, G. Smith, J. Askne, and H. Olsson, "Stem volume estimation in boreal forests using ERS-1/2 coherence and SPOT XS optical data," *Int. J. Remote Sens.*, vol. 22, no. 14, pp. 2777–2791, Jun. 2001.

[14] S. R. Cloude, "Dual-baseline coherence tomography," *IEEE Geosci. Remote Sens. Lett.*, vol. 4, no. 1, pp. 127–131, Jan. 2007.

[15] J. Dall, "InSAR elevation bias caused by penetration into uniform volumes," *IEEE Trans. Geosci. Remote Sens.*, vol. 45, no. 7, pp. 2319–2324, Nov. 2007.

[16] "ERS Missions: 20 Years of Observing Earth," European Space Agency, Noordwijk, Netherlands, ESA SP- 132, Jul. 2013.

[17] D. L. A. Gaveau, "Modelling the dynamics of ERS-1/2 coherence with increasing woody biomass over boreal forests," *Int. J. Remote Sens.*, vol. 23, no. 18, pp. 3879–3885, Jan. 2002.

[18] E. W. Hoen and H. Zebker, "Penetration depths inferred from interferometric volume decorrelation observed over the Greenland ice sheet," *IEEE Trans. Geosci. Remote Sens.*, vol. 38, no. 6, pp. 2571–2583, Nov. 2000.

[19] S. Oveisgharan and H. A. Zebker, "Estimating snow accumulation from InSAR correlation observations," *IEEE Trans. Geosci. Remote Sens.*, vol. 45, no. 1, pp. 10–20, Jan. 2007.

[20] T. Farr *et al.*, "The shuttle radar topography mission," *Rev. Geophys.*, vol. 45, pp. 1–33, 2007.

[21] M. Zink *et al.*, "TanDEM-X: 10 years of formation flying bistatic SAR interferometry," *IEEE J. Sel. Topics Appl. Earth Observ. Remote Sens.*, vol. 14, pp. 3546–3565, Feb. 2021, doi: 10.1109/JSTARS.2021.3062286.

[22] M. Martone, B. Bräutigam, P. Rizzoli, C. Gonzalez, M. Bachmann, and G. Krieger, "Coherence evaluation of TanDEM-X interferometric data," *ISPRS J. Photogrammetry Remote Sens.*, vol. 73, pp. 21–29, Sep. 2012.

[23] P. Rizzoli, M. Martone, and B. Bräutigam, "Global interferometric coherence maps from TanDEM-X quicklook data," *IEEE Geosci. Remote Sens. Lett.*, vol. 11, no. 11, pp. 1861–1865, Nov. 2014.

[24] P. Rizzoli *et al.*, "Generation and performance assessment of the global TanDEM-X digital elevation model," *ISPRS J. Photogrammetry Remote Sens.*, vol. 132, pp. 119–139, Oct. 2017.

[25] F. Kugler, D. Schulze, I. Hajnsek, H. Pretzsch, and K. Papathanassiou, "TanDEM-X Pol-InSAR performance for forest height estimation," *IEEE Trans. Geosci. Remote Sens.*, vol. 52, no. 10, pp. 6404–6422, Oct. 2014.

[26] M. J. Soja, H. Persson, and L. Ulander, "Estimation of forest height and canopy density from a single InSAR correlation coefficient," *IEEE Geosci. Remote Sens. Lett.*, vol. 12, no. 3, pp. 646–650, Mar. 2015.

[27] H. Chen, S. Cloude, and D. G. Goodenough, "Forest canopy height estimation using TanDEM-X coherence data," *IEEE J. Sel. Topics Appl. Earth Observ. Remote Sens.*, vol. 9, no. 7, pp. 3177–3188, Jul. 2016.

[28] A. Olesk, J. Praks, O. Antropov, K. Zalite, T. Arumae, and K. Voormansik, "Interferometric SAR coherence models for characterization of hemiboreal forests using TanDEM-X data," *Remote Sens.*, vol. 8, no. 700, pp. 1–23, Aug. 2016.

[29] H. Chen, S. Cloude, D. G. Goodenough, D. A. Hill, and A. Nesdoly, "Radar forest height estimation in mountainous terrain using TanDEM-X coherence data," *IEEE J. Sel. Topics Appl. Earth Observ. Remote Sens.*, vol. 11, no. 10, pp. 3443–3452, Oct. 2018.

[30] M. Nannini *et al.*, "Coherence-based SAR tomography for spaceborne applications," *Remote Sens. Environ.*, vol. 225, pp. 107–114, Jun. 2019.

[31] M. Schlund, P. Magdon, B. Eaton, C. Aumann, and S. Erasmi, "Canopy height estimation with TanDEM-X in temperate and boreal forests," *Int. J. Appl. Earth Observ. Geoinf.*, vol. 82, Oct. 2019, Art. no. 101904.

[32] R. Guliaev, V. Cazcarra-Bes, M. Pardini, and K. Papathanassiou, "Forest height estimation by means of TanDEM-X InSAR and waveform lidar data," *IEEE J. Sel. Topics Appl. Earth Observ. Remote Sens.*, vol. 14, pp. 3084–3094, Feb. 2021, doi: 10.1109/JSTARS.2021.3058837.

[33] I. H. Askne, E. S. Fransson, M. Santoro, M. J. Soja, and L. M. H. Ulander, "Model-based biomass estimation of a hemi-boreal forest from multitemporal TanDEM-X acquisitions," *Remote Sens.*, vol. 5, no. 11, pp. 5574–5597, Oct. 2013.

[34] R. Treuhaft *et al.*, "Tropical-forest biomass estimation at X-band from the spaceborne TanDEM-X interferometer," *IEEE Geosci. Remote Sens. Lett.*, vol. 12, no. 2, pp. 239–243, Feb. 2015.

[35] W. Qi and R. O. Dubayah, "Combining TanDEM-X InSAR and simulated GEDI lidar observations for forest structure mapping," *Remote Sens. Environ.*, vol. 187, pp. 253–266, Dec. 2016.

[36] J. Askne, M. Soja, and L. Ulander, "Biomass estimation in a boreal forest from TanDEM-X data, lidar DTM, and the interferometric water cloud model," *Remote Sens. Environ.*, vol. 196, pp. 265–278, Jul. 2017.

[37] H. Persson, M. Soja, J. Fransson, and M. Ulander, "National forest biomass mapping using the two-level model," *IEEE J. Sel. Topics Appl. Earth Observ. Remote Sens.*, vol. 13, pp. 6391–6400, Oct. 2020, doi: 10.1109/JSTARS.2020.3030591.

[38] E. Erten, C. Rossi, and O. Yüzügüllü, "Polarization impact in TanDEM-X data over vertical-oriented vegetation: The paddy-rice case study," *IEEE Geosci. Remote Sens. Lett.*, vol. 12, no. 7, pp. 1501–1505, Jul. 2015.

[39] J. Lopez-Sanchez, F. Vicente-Guijalba, E. Erten, M. Campos-Taberner, and F. Garcia-Haro, "Retrieval of vegetation height in rice fields using polarimetric SAR interferometry with TanDEM-X data," *Remote Sens. Environ.*, vol. 192, pp. 30–44, Apr. 2017.

[40] M. Busquier, J. Lopez-Sanchez, A. Mestre-Quereda, E. Navarro, M. Gonzalez-Dugo, and L. Mateos, "Exploring TanDEM-X interferometric products for crop-type mapping," *Remote Sens.*, vol. 12, no. 11, Jun. 2020, Art. no. 1774, doi: 10.3390/rs12111774.

[41] M. Schlund, F. von Poncet, D. H. Hoeckman, S. Kuntz, and C. Schmullius, "Importance of bistatic SAR features from TanDEM-X for forest mapping and monitoring," *Remote Sens. Environ.*, vol. 151, pp. 16–26, Aug. 2014.

[42] M. Martone *et al.*, "The global forest/non-forest map from TanDEM-X interferometric SAR data," *Remote Sens. Environ.*, vol. 205, pp. 352–373, Feb. 2018.

[43] M. Martone, F. Sica, C. Gonzalez, J.-L. Bueso-Bello, P. Valdo, and P. Rizzoli, "High-resolution forest mapping from TanDEM-X interferometric data exploiting nonlocal filtering," *Remote Sens.*, vol. 10, no. 9, Sep. 2018, Art. no. 1477, doi: 10.3390/rs10091477.

[44] A. Mazza, F. Sica, P. Rizzoli, and G. Scarpa, "TanDEM-X forest mapping using convolutional neural networks," *Remote Sens.*, vol. 11, 2019, Art. no. 2980, doi: 10.3390/rs11242980.

[45] P. Rizzoli, M. Martone, H. Rott, and A. Moreira, "Characterization of snow facies on the Greenland ice sheet observed by TanDEM-X interferometric SAR data," *Remote Sens.*, vol. 9, no. 4, Mar. 2017.

[46] G. Fischer, K. Papathanassiou, and I. Hajnsek, "Modeling multifrequency Pol-InSAR data from the percolation zone of the Greenland ice sheet," *IEEE Trans. Geosci. Remote Sens.*, vol. 57, no. 4, pp. 1963–1976, Apr. 2019.

[47] S. Abdullahi, B. Wessel, M. Huber, A. Wendleder, A. Roth, and C. Kuenzer, "Estimating penetration-related x-band InSAR elevation bias: A study over the Greenland ice sheet," *Remote Sens.*, vol. 11, 2019, Art. no. 2903, doi: 10.3390/rs11242903.

[48] H. Rott *et al.*, "Penetration of interferometric radar signals in antarctic snow," *Cryosphere*, vol. 15, pp. 4399–4419, Sep. 2021.

[49] R. Kwok and W. T. K. Johnson, "Block adaptive quantization of magellan SAR data," *IEEE Geosci. Remote Sens. Lett.*, vol. 27, no. 4, pp. 375–383, Jul. 1989.

[50] R. K. Raney, A. Freeman, R. W. Hawkins, and R. Bamler, "A plea for radar brightness," *Proc. Int. Geosci. Remote Sens. Symp.*, vol. 2, pp. 1090–1090, 1994.

[51] *TerraSAR-X Ground Segment—Level 1b Product Format Specification*, DLR public document TX-GS-DD-3307, Dec. 2007.

[52] F. Ulaby and M. Craig Dobson, *Handbook of Radar Scattering Statistics for Terrain*. Norwood, MA, USA: Artech, 1989.

[53] J.-L. Bueso-Bello *et al.*, "The Global water body layer from TanDEM-X interferometric SAR data," *Remote Sens.*, vol. 13, Dec. 2021, Art. no. 5069, doi: 10.3390/rs13245069.

[54] C. Gonzalez, M. Bachmann, J. Bueso-Bello, P. Rizzoli, and M. Zink, "A fully automatic algorithm for editing the TanDEM-X global DEM," *Remote Sens.*, vol. 12, no. 23, Dec. 2020, Art. no. 3961, doi: 10.3390/rs12233961.

[55] *TanDEM-X Ground Segment—Experimental Product Description*, DLR public document TD-GS-PS-3028, Jan. 2012.

[56] M. Martone, N. Gollin, P. Rizzoli, and G. Krieger, "Performance-optimized quantization for InSAR applications," in *Proc. 13th Eur. Conf. Synthetic Aperture Radar*, Mar. 2021, pp. 1–6.

[57] A. Becker, S. Russo, S. Puliti, N. Langa, K. Schindler, and J. D. Wegner, "Country-wide retrieval of forest structure from optical and SAR satellite imagery with Bayesian deep learning," *arXiv:2111.13154v1*, 2021.

Paola Rizzoli received the B.Sc. and M.Sc. degrees in telecommunication engineering from the Politecnico di Milano University (Polimi), Milan, Italy, in 2003 and 2006, respectively, and the Ph.D. degree *(summa cum laude)* in electrical engineering and information technology from the Karlsruhe Institute of Technology (KIT), Karlsruhe, Germany, in 2018.

From 2006 to 2008, she was with the Politecnico di Milano and Aresys s.r.l., a Polimi spin-off company, as a Scientific Researcher and Project Engineer. At the end of 2008, she joined the Microwaves and Radar Institute, German Aerospace Center (DLR), Oberpaffenhofen, Germany, as a Project Engineer, where she has been involved in the development and optimization of the TerraSAR-X and TanDEM-X missions, concentrating, in particular, on the generation of the TanDEM-X global digital elevation model. From 2016 to 2020, she led the System Performance Research Group, Satellite SAR Systems Department, being responsible for the final performance assessment of the global TanDEM-X DEM and the generation of the global TanDEM-X Forest/Non-Forest map. Since 2020, she has been leading the Radar Science Research Group, DLR. Her main research interests include SAR systems design, data reduction techniques, estimation theory, signal processing, and artificial intelligence algorithms.

Dr. Rizzoli was the recipient of the DLR Science Award in 2018 and the Best Paper Award at the German Microwave Conference in 2019. She regularly serves as a Reviewer for the IEEE TRANSACTIONS ON GEOSCIENCE AND REMOTE SENSING, IEEE GEOSCIENCE AND REMOTE SENSING LETTERS, and IEEE JOURNAL OF SELECTED TOPICS IN APPLIED EARTH OBSERVATIONS AND REMOTE SENSING.

Luca Dell'Amore received the M.Sc. degree in information and communication engineering from the Università degli Studi di Trento, Trento, Italy, in 2019. His master thesis was titled "Assessment of Image Quality of Waveform-Encoded Synthetic Aperture Radar (SAR) Using Real Data."

In 2019, he was awarded a German Academic Exchange Service (DAAD) Scholarship for a Doctorate in the Radar Concepts Department, Microwaves and Radar Institute, DLR, where since 2021, he has been with the Satellite SAR Systems Department, as a Research Engineer. He is currently working on performance investigation for the TerraSAR-X and TanDEM-X missions. His main research interests include the investigation of distributed SAR systems, with a particular focus on multiple-input–multiple-output SAR, and the development of innovative methods for performance monitoring using Sentinel-1 data.

José-Luis Bueso-Bello received the Ingeniero degree in telecommunications engineering from the Universidad Politecnica de Valencia, Valencia, Spain, in 2003, and the M.Sc. degree in Earth-oriented space science and technology from the Technische Universität München, Munich, Germany, in 2007.

In 2003, he was a System Engineer with the Department of Reconnaissance and Security, Microwaves and Radar Institute, German Aerospace Center (DLR), Oberpfaffenhofen, Germany, where he worked on the definition, design, and mission analysis for different SAR Projects. In 2010, he joined the Satellite SAR Systems Department, where he is currently a Performance Engineer with main focus on the TerraSAR-X and TanDEM-X Projects. His main research interests include performance analysis and image quality assessment of actual and future radar systems, together with remote sensing applications related to large-scale land cover mapping.

Nicola Gollin received the M.Sc. degree in information and communication engineering from the Università degli Studi di Trento, Trento, Italy, in 2018. His master thesis was on predictive quantization for data volume reduction in staggered synthetic aperture radar (SAR) systems.

Since 2018, he has been with the System Performance Group, Microwaves and Radar Institute, DLR, where he is currently a Project Engineer. His research interests include signal processing applied to synthetic aperture radar, and the analysis and design of future SAR systems.

Mr. Gollin was the recipient of the Best Paper Award at the German Microwave Conference and the ARGUS Science Award, both in 2019.

Daniel Carcereri received the M.Sc. degree in information and communication engineering from the University of Trento, Trento, Italy, in 2020. His master thesis was on quantization error reduction in synthetic aperture radar (SAR) systems. He is currently working toward the Ph.D. degree with the Remote Sensing Laboratory, Department of Information and Communication Technology, University of Trento and the Microwaves and Radar Institute, German Aerospace Center, Wessling, Germany.

His research interests include sensor fusion and deep learning algorithms applied to forest parameter estimation and analysis.

Michele Martone received the B.Sc. and M.Sc. degrees in telecommunication engineering from the University of Naples Federico II, Naples, Italy, in 2006 and 2009, respectively, and the Ph.D. degree in electrical engineering and information technology from the Karlsruhe Institute of Technology, Karlsruhe, Germany, in 2019 .

Since 2009, he has been with the Microwaves and Radar Institute, German Aerospace Center (DLR), Weling, Germany, where he has participated in the development and optimization of the TerraSAR-X and TanDEM-X spaceborne SAR missions, the generation of the global TanDEM-X digital elevation model and Forest/Non-Forest map, and has been involved in several projects in collaboration with research and industry partners focused on the design of future SAR missions. He has authored or coauthored nearly 100 research articles in peer-reviewed journals and international conference proceedings and holds two patents in the field of SAR. His research interests include the conception of innovative SAR systems with particular focus on the development of efficient quantization and data volume reduction methods.

Dr. Martone has been a Member of Technical Program Committee for several international conferences and workshops. He was the recipient of the DLR Science Award in 2018 and the Best Paper Award at the German Microwave Conference 2019. He regularly serves as a Reviewer for IEEE TRANSACTIONS ON GEOSCIENCE AND REMOTE SENSING, IEEE GEOSCIENCE AND REMOTE SENSING LETTERS, and IEEE JOURNAL OF SELECTED TOPICS IN APPLIED EARTH OBSERVATIONS AND REMOTE SENSING.